# New phenomena in variable-density Rayleigh–Taylor turbulence

## D Livescu, J R Ristorcelli, M R Petersen and R A Gore

Los Alamos National Laboratory, Los Alamos, NM 87545, USA

E-mail: livescu@lanl.gov

## Abstract

This paper presents several issues related to mixing and turbulence structure in
buoyancy-driven turbulence at low to moderate Atwood numbers, $A$, found from direct
numerical simulations in two configurations: classical Rayleigh–Taylor instability and an
idealized triply periodic Rayleigh–Taylor flow. Simulations at $A$ up to 0.5 are used to examine
the turbulence characteristics and contrast them with those obtained close to the Boussinesq
approximation. The data sets used represent the largest simulations to date in each
configuration. One of the more remarkable issues explored, first reported in (Livescu and
Ristorcelli 2008 *J. Fluid Mech.* **605** 145–80), is the marked difference in mixing between
different density fluids as opposed to the mixing that occurs between fluids of commensurate
densities, corresponding to the Boussinesq approximation. Thus, in the triply periodic
configuration and the non-Boussinesq case, an initially symmetric density probability density
function becomes skewed, showing that the mixing is asymmetric, with pure heavy fluid
mixing more slowly than pure light fluid. A mechanism producing the mixing asymmetry is
proposed and the consequences for the classical Rayleigh–Taylor configuration are discussed.
In addition, it is shown that anomalous small-scale anisotropy found in the homogeneous
configuration (Livescu and Ristorcelli 2008 *J. Fluid Mech.* **605** 145–80) and Rayleigh–Taylor
turbulence at $A = 0.5$ (Livescu *et al* 2008 *J. Turbul.* **10** 1–32) also occurs near the Boussinesq
limit. Results pertaining to the moment closure modelling of Rayleigh–Taylor turbulence are
also presented. Although the Rayleigh–Taylor mixing layer width reaches self-similar growth
relatively fast, the lower-order terms in the self-similar expressions for turbulence moments
have long-lasting effects and derived quantities, such as the turbulent Reynolds number, are
slow to follow the self-similar predictions. Since eddy diffusivity in the popular gradient
transport hypothesis is proportional to the turbulent Reynolds number, the dissipation rate and
turbulent transport have different length scales long after the onset of the self-similar growth
for the layer growth. To highlight the importance of turbulent transport, variable density
energy budgets for the kinetic energy, mass flux and density-specific volume covariance
equations, necessary for a moment closure of the flow, are provided.

PACS numbers: 47.20.-k, 42.20.E-, 47.55.P-, 47.27.wj

## 1. Introduction

Variable density (VD) flows generally denote flows involving
mixing between fluids with different densities, in contrast to
the Boussinesq approximation in which the fluids' densities
are closed. In such flows, even if the fluids participating in the
mixing are incompressible, the density and specific volume
change with the mixture composition and the velocity field
is not divergence free. Moreover, due to the tight coupling
between the density and velocity fields, in addition to the

quadratic nonlinearities of the incompressible Navier–Stokes
equations, new cubic nonlinearities arise. VD mixing occurs
in atmospheric and oceanic flows, astrophysical flows,
combustion and many flows relating to chemical engineering.
Many of these flows are driven by acceleration (e.g. gravity
in geophysical and astrophysical flows) which, because the
density is not uniform, leads to large differential fluid
accelerations. If the acceleration is constant and the fluid
configuration is unstable (i.e. density gradient points in the
opposite direction to the body force), a fluid instability

is generated in which small perturbations of the initial interface between the two fluids grow, interact nonlinearly and lead to turbulence. This instability is known as the Rayleigh–Taylor (RT) instability and is of fundamental importance in a multitude of applications, from fluidized beds, oceans and atmosphere, to inertial confinement fusion (ICF) and supernovae (see [1–12] for useful reviews and open problems).

Here, we study the homogenization of a heterogeneous mixture of two pure fluids with constant, but different, microscopic densities by molecular diffusion and stirring induced by buoyancy-generated motions. The specific volume and density of the mixture are related to the microscopic densities, $\rho_l$, and mass fractions, $Y_l^*$, $l = 1, 2$, of the two pure fluids by

$$v^* = \frac{1}{\rho^*} = \frac{Y_1^*}{\rho_1} + \frac{Y_2^*}{\rho_2}, \tag{1}$$

where $Y_1^* + Y_2^* = 1$. The index '2' refers to the heavier fluid. The mixture density, $\rho^*$, and the specific volume, $v^*$, change in both space and time as the mass fractions evolve and the relation above simply states that the total mass inside a control volume is the sum of the masses of the two fluids. Such a configuration describes active mixing, at any density ratio, between incompressible materials (e.g. water and brine) or compressible materials in low-speed, low-acceleration flows when the fluids participating in the mixing maintain quasi-constant microscopic densities.

The primary non-dimensional parameter characterizing differential acceleration effects is the Atwood number:

$$A \equiv \frac{\rho_2 - \rho_1}{\rho_2 + \rho_1} \Rightarrow \frac{\rho_2}{\rho_1} = \frac{1 + A}{1 - A}. \tag{2}$$

The Atwood number ranges from 0 to 1. For air interpenetrating helium, for which the density ratio is $\rho_2/\rho_1 \approx 7$, the Atwood number is $A \approx 0.75$. For air and hydrogen, $A = 0.85$. Similar Atwood numbers occur for mixing between liquid hydrocarbons and air. In contrast, the Boussinesq approximation corresponds to $A \rightarrow 0$ and a value of 0.05 is usually taken to define this limit.

The goal of the paper is to provide an overview of the VD effects in buoyancy-driven turbulence at low to moderate Atwood numbers, including unexpected new phenomena related to mixing and turbulence structure. These effects are considered in two unit configurations: (i) classical RT instability and (ii) an idealized triply periodic RT flow, named homogeneous RT (HRT). The data sets used represent the largest simulations to date for each configuration. For the RT case, a $3072^3$ data set [2, 4] at $A = 0.5$ is contrasted with a new $1024^2 \times 4032$ fully resolved simulation at $A = 0.04$ near the Boussinesq approximation. The HRT flow starts from rest, with the two fluids in a non-premixed state corresponding to a double-delta density probability density function (PDF). Turbulence is generated as the two fluids move in opposite directions due to the body force and eventually dies as the fluids become molecularly mixed. The cases considered, on up to $1024^3$ meshes [1, 3], cover the range $A = 0.05$–$0.5$, in order to examine small departures from the Boussinesq approximation as well as moderate $A$ effects. Although some

of the results pertaining to the $3072^3$ run have already been presented in [2], they are reviewed here and compared to the new simulation near the Boussinesq limit. There are two reasons for this. Firstly, direct comparison provides a uniform view of the differences and similarities between VD and Boussinesq flows. Secondly, direct numerical simulations (DNS) of the RT instability are scarce and the vast majority of RT simulations actually solve the Euler equations and rely on numerical diffusion to regularize the problem. Thus, new DNS results obtained with a different code can confirm previous results.

The paper is organized as follows. The governing equations, initial conditions, simulation parameters and numerical methodology are described in section 2. Section 3 addresses the self-similarity of the flow, turbulence asymmetry due to non-Boussinesq effects, large- and small-scale anisotropies, second moment budget equations, measures for the mixing state, and mixing asymmetry in VD turbulence. A summary and conclusions are given in section 4.

## 2. Governing equations, simulation cases and numerical method

The flows in the two configurations considered are governed by the same set of equations: continuity, momentum transport and the velocity divergence relation related to the density field. In non-dimensional form, these are [2–4, 13–15]:

$$\frac{\partial}{\partial t} \rho^* + (\rho^* u_j^*)_{,j} = 0, \tag{3}$$

$$\frac{\partial}{\partial t}(\rho^* u_i^*) + (\rho^* u_i^* u_j^*)_{,j} = -p_{,i}^* + \tau_{ij,j}^* + \frac{1}{Fr^2} \rho^* g_i, \tag{4}$$

$$u_{j,j}^* = -\frac{1}{Re_0 Sc}(\ln \rho^*)_{,jj}, \tag{5}$$

where $^*$ denotes total (instantaneous) variables. The viscous stress is Newtonian with

$$\tau_{ij}^* = \frac{\rho^*}{Re_0}\left[ u_{i,j}^* + u_{j,i}^* - \frac{2}{3}u_{k,k}^* \delta_{ij} \right] \tag{6}$$

and the mass diffusion Fickian, with constant diffusion coefficient, $\mathcal{D}$. Note that equations (3) and (4) are the usual continuity and momentum transport equations for compressible flows. Equation (5) is derived from the usual mass fraction transport equations, assuming that the microscopic densities of the two fluids remain constant, which relates the mass fractions to the density (see equation (1)) [3, 13, 15]. Equations (3)–(5) describe the mixing, at any density ratio, between incompressible materials (e.g. water and brine) or compressible materials in low-speed, low-acceleration flows, when the fluids participating in the mixing maintain quasi-constant microscopic densities. If the densities of the two fluids are commensurate, then the mixture density is close to its average value and equations (3)–(5) lead to the Boussinesq approximation (see [3] for the derivation).

In equations (3)–(5), $u_i^*$ is the velocity in direction $i$, $\rho^*$ is mixture density and $p^*$ is pressure. The non-dimensional

parameters in equations (3)–(5) are the computational Reynolds number, $Re_0$, the Schmidt number, $Sc$, and the Froude number, $Fr$:

$$Re_0 = L_0 U_0 / \nu_0, \quad Sc = \nu_0 \mathcal{D}, \quad Fr^2 = U_0^2 / (g L_0), \quad (7)$$

with $g$ being the magnitude of gravitational acceleration, taken to be constant. Here $g_i$ are the components of the unit vector in the direction of gravity, $g_i = (0, 0, -1)$. The independent variables are time $t$ and space variables $x_i$. The kinematic viscosity, $\nu_0 = \mu / \rho^*$, and mass diffusion coefficient, $\mathcal{D}$, are assumed to be constant. Note that, in general, dynamic viscosity, $\mu$, is a weaker function of density; the assumption of $\nu_0$ as constant ensures a uniform $Sc$ throughout the flow. The reference density, $\rho_0$, is chosen such that the density of the light fluid is 1.0 and the reference length and velocity are specified below.

Equations (3)–(5) have triply periodic boundary conditions in HRT, whereas in RT slip wall conditions are applied in the vertical direction.

### 2.1. Simulation cases and numerical method

In order to examine the VD effects on the turbulence and mixing characteristics in buoyancy-driven flows, simulations from [1, 3], with $A = 0.05$, 0.25 and 0.5 and $Sc = 1$, are considered for HRT. For RT, the $3072^3$ simulation of Cabot and Cook [2, 4], at $A = 0.5$, is complemented with a new simulation, at $A = 0.04$, on a $1024^2 \times 4032$ mesh. For simplicity, the two runs are labeled RT1 ($A = 0.5$) and RT2 ($A = 0.04$). In order to compare the two RT runs, the reference length and time scales are defined as the characteristic wavelength of the initial perturbation spectrum, $L_0$, and $\tau = \sqrt{L_0 / (Ag)}$. The resulting values are $L_0 = 32$ and $\tau = 8$ for RT1 [4] and $L_0 = 0.196$ and $\tau = 0.16$ for RT2. The reference velocity is then $U_0 = L_0 / \tau$.

The new RT simulation was performed with the CFDNS code [16]. The numerical method and initialization are similar to those used in [4, 13] with several differences as pointed out below. Thus, spatial differentiation is performed with a sixth-order compact finite difference scheme [17] in the vertical direction (compared to the tenth-order compact finite difference scheme used in [4, 13]) and in Fourier space in the horizontal (periodic) directions. To account for the difference in accuracy between the compact finite difference scheme and the Fourier differentiation, the grid spacing is 25% smaller in the vertical direction. For this grid size, the error at the Kolmogorov microscale is about 1% for the compact method, if $\eta k_{max}$ is maintained above 1.5 [18]. Nevertheless, since the Kolmogorov microscale is not well defined for inhomogeneous flows, resolution studies were performed to verify that the solution converged. In addition, the velocity and density power spectra were monitored during the simulation to ensure that all scales were well resolved.

The time integration was performed with a third-order predictor–corrector Adams–Bashforth–Moulton scheme coupled with a pressure projection method, similar to [4, 13]. The main difference lies in how the pressure equation was handled. The VD equations lead to a variable coefficient (non-linear) Poisson equation for pressure, as shown in [3]. This equation was split into an explicit equation for the dilatational component of $\nabla P^* / \rho^*$, which is related to mass conservation, and an implicit equation for the solenoidal (curl) component of $\nabla P^* / \rho^*$, which is related to the baroclinic term in the vorticity equation [3, 15]. Instead of interpolating the velocity from the previous time step to solve the pressure equation, as was done in [4, 13], the pressure equation was solved without additional approximations. This avoided the introduction of errors of the same order as the interpolation method in both mass conservation and baroclinic production of vorticity. The specific solution method extends the algorithms used in [3, 15] for HRT to the RT configuration and will be described in detail elsewhere.

### 2.2. Nomenclature

In defining the turbulence quantities, capital Roman letters, overbars and angle brackets are used to denote Reynolds averages. Angle brackets are preferred for longer expressions, while overbars are used for quantities named with Greek letters. Lower case letters (Roman or Greek) or primes are used to denote fluctuations. One exception is the mix measure $\theta$ for which the usual definition has been adopted. As the density is not spatially uniform, some of the results are presented using density weighted (Favre) averages, denoted with ~, and the corresponding fluctuations with double primes. Thus, the instantaneous velocity, density, pressure and specific volume are decomposed as $u_i^* = U_i + u_i = \tilde{U}_i + u_i''$, $\rho^* = \overline{\rho} + \rho$, $p^* = P + p$, and $v^* = V + v$, respectively. Note that $\tilde{U}_i - U_i = u_i - u_i'' = a_i$. Definitions for the normalized mass flux, $a_i$, Favre Reynolds stresses, $R_{ij}$, turbulent kinetic energy, $\tilde{k}$, total kinetic energy, $E_K$, and density specific volume covariance, $b$, are given below:

$$a_i = \frac{\langle u_i \rho \rangle}{\overline{\rho}} = -\langle u_i'' \rangle, \quad (8)$$

$$R_{ij} = \langle \rho^* u_i'' u_j'' \rangle = \overline{\rho} \langle u_i u_j \rangle - \overline{\rho} a_i a_j + \langle \rho u_i u_j \rangle, \quad (9)$$

$$\tilde{k} = R_{kk} / (2\overline{\rho}) = (\langle u_i u_i \rangle - a_i a_i + \langle \rho u_i u_i \rangle / \overline{\rho}) / 2, \quad (10)$$

$$E_K = \langle \rho^* u_i^* u_i^* \rangle / 2 = (\overline{\rho} \langle u_i u_i \rangle + \langle \rho u_i u_i \rangle) / 2 = \overline{\rho}(\tilde{k} + \tilde{K}), \quad (11)$$

$$b = -\langle \rho v \rangle. \quad (12)$$

## 3. Results

### 3.1. RT self-similarity

The temporal evolution of the RT layer width is an important question in applications and can be regarded as a metric to gauge the efficacy of various models and numerical simulations. Although certain classes of initial conditions (e.g. if long wavelengths are present in the initial perturbation) may have a long-lasting influence on the growth rate [10, 19], it is generally agreed that for (i) domains long horizontally
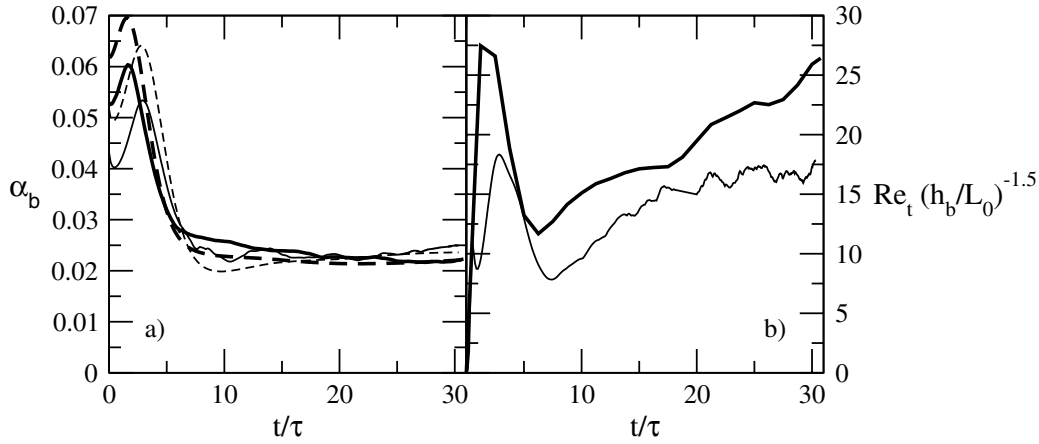
**Figure 1.** (a) Time variation of $\alpha_b$ for RT1 (thick lines) and RT2 (thin lines) using (14), with $t_0/\tau = 6$ and 7.5, respectively, for the bubble height calculated from the 1% density level (continuous lines) and $\beta W$ (dashed lines). (b) Evolution of the peak turbulent Reynolds number times $(h_b/L_0)^{-1.5}$. Self-similarity of $Re_t$ requires that it grows as $(h_b/L_0)^{1.5}$.

compared to any characteristic wavelength of the perturbation and (ii) much longer in the vertical direction than the width of the layer, and for (iii) an initial perturbation spectrum peaked near the most unstable linear mode, the turbulent-mixing layer grows quadratically in time. This quadratic growth has been known for a long time as a dimensionally consistent result confirmed by experimental data [20–22]. Ristorcelli and Clark [9] provided the first analytical derivation of the self-similar formula for the layer width, using the moments equations:

$$h = \alpha A g t^2 + 2(\alpha A g h_0)^{1/2} t + h_0. \quad (13)$$

Although asymptotically the leading order term in equation (13) should dominate, the onset of self-similarity of the mixing layer width growth occurs much earlier. Nevertheless, in order to calculate the value of the coefficient $\alpha$ before the flow reaches asymptotic self-similarity, the lower-order terms in equation (13) need to be properly accounted for. Cabot and Cook [4] used a formula consistent with the underlying self-similar differential equation for $h$, $\alpha_{CC} = \dot{h}^2/4Agh$. However, the time derivative of $h$ may lead to excessive noise in the value of $\alpha$, especially if the data are sparse. Another formula for $\alpha$, which avoids the time derivative but is still derived from equation (13), is

$$\alpha = \left( \frac{h(t)^{1/2} - h(t_0)^{1/2}}{(Ag)^{1/2}(t - t_0)} \right)^2, \quad (14)$$

where $t_0$ is an arbitrary time within the self-similar range. For the miscible case, there is no unique definition of $h$. Thus, Cabot and Cook [4] use $h = \int_{-\infty}^{\infty} X_P(\bar{\rho}) \mathrm{d}z$, where $X_P(\bar{\rho})$ is the maximum product in a fast reaction analogy [1, 13]. Youngs ([12, 23] and references therein) uses the definition $W = \int_{-\infty}^{\infty} F_1 F_2 \, \mathrm{d}z$, where $F_1 = (\bar{\rho} - \rho_1)/(\rho_2 - \rho_1)$ and $F_2 = (\rho_2 - \bar{\rho})/(\rho_2 - \rho_1)$ are the averages (over horizontal planes) of the volume fractions occupied by the two fluids. Other definitions include the widths based on the 1% and 5% density levels, $H_{0.01}$ and $H_{0.05}$ [2]. Figure 1(a) shows the variation of $\alpha_b$ for the bubble height based on the 1% density level, and $h_b = \beta W$, where the coefficient $\beta = 3.3$ at $A = 0.5$ and

$\beta = 3.7$ at $A = 0.04$, accounts for the diffuse variation of the volume fraction near the edges of the layer (a value of 3 corresponds to linear variation). The values obtained for $\alpha_b$ are within the range obtained in previous numerical simulations [10, 12] corresponding to short-wavelength initial perturbations such that the mode coupling and the growth at the infrared end of the energy spectrum are unrestricted.

However, even though the layer width becomes self-similar relatively fast, the lower-order contributions to the self-similar relations have a long-lasting influence. Thus, certain derived quantities, such as the turbulent Reynolds number, $Re_t = Re_0 \tilde{k}^2/\epsilon$, did not reach self-similarity in RT1 [2]. The reason for this is mismatch between the lower-order terms in the self-similar formulae for the kinetic energy and dissipation. The behavior can also be associated with a lag in the self-similar evolution of the small-scales, compared to the large-scales. The RT2 results shown in figure 1(b) confirm this behavior near the Boussinesq limit. Towards the end of the RT2 simulation, $Re_t$ becomes self-similar, indicating that the flow is close to asymptotic self-similarity. Nevertheless, the approach to full self-similarity occurs much later than the time the layer width starts growing self-similarly. Since $Re_t$ is proportional to eddy diffusivity in the popular gradient diffusion hypothesis for turbulent transport, the lack of temporal self-similarity of the turbulent Reynolds number renders such a modelling approach inappropriate before full self-similarity is reached (see [2] for a detailed discussion). In addition, the onset of self-similar growth for the layer width is a poor indicator of asymptotic self-similarity. In order to use the gradient transport hypothesis for turbulent transport before asymptotic self-similarity is reached, the lengthscales associated with the dissipation and turbulent transport terms in the moments equations cannot be proportional. The results presented here suggest that low and moderate Atwood number RT turbulence are similar in this regard.

### 3.2. Turbulence structure

In this section, the results pertaining to the turbulence asymmetry due to non-Boussinesq effects, large- and small-scale anisotropies, including the anomalous small-scale
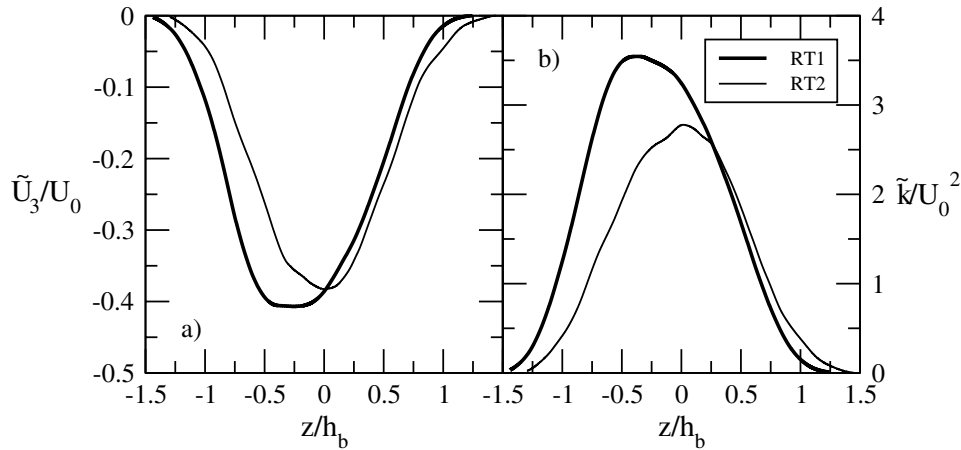
4

**Figure 2.** (a) Favre mean velocity and (b) Favre turbulent kinetic energy variation across the layer for RT1 (thick lines) and RT2 (thin lines) at the latest times in the simulations. For clarity the RT2 results are multiplied by a factor of 20 for $\tilde{U}/U_0$ and a factor of 2 for $\tilde{k}/U_0^2$.
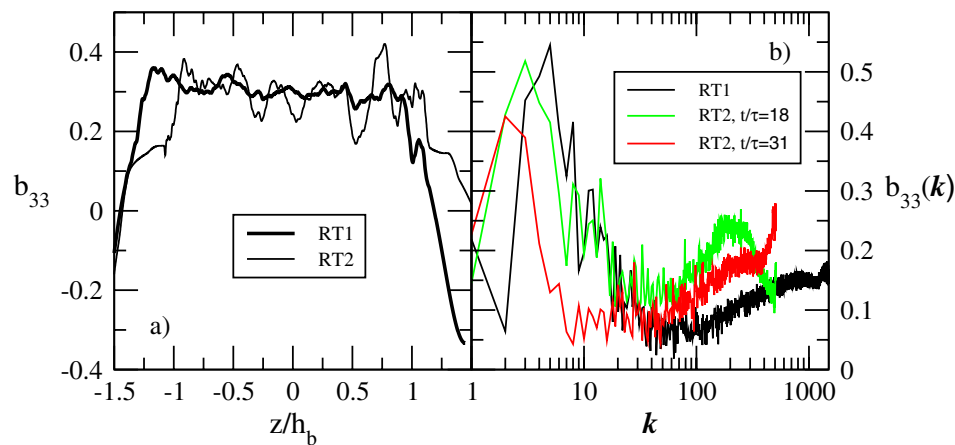


**Figure 3.** (a) Vertical variation of $b_{33}$ and (b) scale dependence of the normal stresses anisotropy at the centerline for RT1, at the latest time and RT2, at the latest time and also some intermediate time.

anisotropy found in [1, 2], and the second moment equations budgets studied in [2] are reviewed and compared to those obtained near the Boussinesq limit.

*3.2.1. Turbulence asymmetry.* At low Atwood numbers, the mixing layer remains symmetrical around the centerline and the mean pressure is equal to the hydrostatic pressure head. As the Atwood number is increased and the flow becomes non-Boussinesq, the bubble and spike sides start to differentiate, with the spikes falling faster than the ascending velocity of the bubbles [7]. Nevertheless, at moderate $A$, the mean density profile remains linear and symmetrical with respect to the centerline in the interior of the layer. From here, it was shown in [2] that self-similarity requires that the mean density keeps a constant value in time at the centerline, after the initial transients. Then, from the mean continuity equation, $\bar{\rho}\tilde{U}$ peaks at the centerline, so that $\tilde{U}$ has the largest absolute value on the light fluid side. This asymmetry, together with mean pressure asymmetric departure from the hydrostatic pressure head, leads to a host of other asymmetries of many turbulence quantities. Since the leading causes of turbulence asymmetry are the asymmetry of the mean density profile itself and the non-Boussinesq behavior of the mean pressure, turbulence asymmetry should increase with $A$ and vanish near the Boussinesq limit. Indeed, figure 2 shows that both $\tilde{U}$ and

$\tilde{k}$ are fairly symmetric across the layer at $A = 0.04$, but both peak on the light fluid side at $A = 0.5$.

*3.2.2. Large- and small-scale anisotropy.* Since buoyancy production is inherently anisotropic, it is expected that the normal stresses be anisotropic. A measure of the large-scale anisotropy, which appears in the moment equations, is the Favre Reynolds stress anisotropy tensor:

$$b_{ij} = \frac{R_{ij}}{R_{kk}} - \frac{1}{3}\delta_{ij}, \tag{15}$$

which is bounded by $-\frac{1}{3} \leqslant b_{ij} \leqslant \frac{2}{3}$. The lower bound for a diagonal component corresponds to no energy in that component and the upper bound, $\frac{2}{3}$, to 100% of the energy in that component. Both simulations show that the normal stresses are anisotropic at all times. Note that for the present configuration, as well as HRT, $b_{ij}$ defined based on the Favre Reynolds stresses is close to that defined based on the Reynolds stresses. $b_{33}$ seems to become almost constant across the layer, with an asymptotic value $b_{33} \approx 0.3$ (figure 3(a)) corresponding to $\approx 65\%$ energy in the vertical component. Values of $b_{33} \approx 0.3$ were also reported for the Boussinesq case at long times at the centerline in [9]. Similar values are obtained in HRT during the growth stage, after initial transients [1, 3].
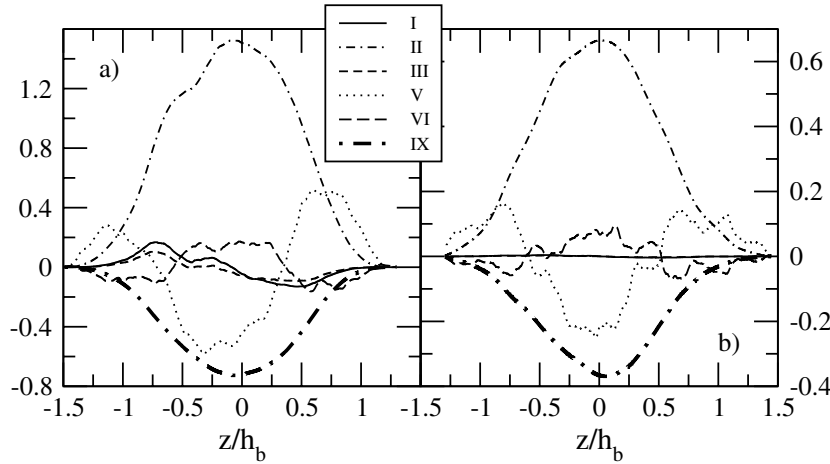
**Figure 4.** Terms in the Favre turbulent kinetic energy equation, scaled by $\tau^3/L_0^2$, for (a) RT1 and (b) RT2.

It is generally believed that in high Reynolds number flows, the small scales become isotropic and decoupled from the large scales as, in general, production mechanisms tend to be confined to large scales. However, in [1], it was shown that buoyancy production, even though it becomes much smaller than the nonlinear transfer at high wavenumbers, has a significant effect on the smallest scales of the flow during the kinetic energy growth stages in HRT. This is because in the viscous range there is a cancellation between nonlinear transfer and viscous dissipation so that buoyancy production leads to anomalous anisotropy of the normal stresses at these scales. The results regarding anisotropy found in HRT [1, 3] were shown to hold in the RT configuration at $A = 0.5$ [2] and later confirmed in the stationary VD simulations of [15]: the normal stresses tend to become isotropic only at intermediate scales. At the largest and smallest scales, the normal stresses remain anisotropic. Figure 3(b) shows that this is not strictly a VD effect. The low Atwood number simulation RT2 exhibits a similar behavior, with reduced anisotropy in some intermediate range of scales and an increase at the small scales. The RT2 results also show that in time, as the Kolmogorov scale decreases, the small-scale anisotropic region moves to the right in spectral space. At the end of the two simulations, the small-scales anisotropy peak reaches the end of the spectrum, suggesting that in both situations this feature starts to become under-resolved. Although the Taylor–Reynolds number and the Kolmogorov microscale are not well defined for inhomogeneous flows, we note that using the isotropic formulae leads to $Re_\lambda \approx 170$ and 150 and $\eta k_{\max} \approx 6.0$ and 3.5 for RT1 and RT2, respectively. Thus, in order to capture the anomalous small-scale anisotropy, much more resolution is needed than usually assumed to be sufficient for canonical isotropic turbulence simulations. At the end of RT1 and RT2, $b_{33}(\kappa)$ reaches values of 0.15 and 0.25, corresponding to $\approx 50\%$ and $\approx 60\%$ energy in the vertical component for RT1 and RT2, respectively. These values are close to those obtained in HRT at similar $A$ and $Sc$. We also note that dissipation itself is not a good measure of the local (in scale) anisotropy as it is an integral quantity; for both the simulations presented here, dissipation becomes isotropic at later times.

### 3.3. Energy budgets of the second moments equations

The energy budgets for the Favre turbulent kinetic energy, $\tilde{k}$, normalized mass flux, $a_i$, and density specific volume correlation, $b$, transport equations are now examined. These equations are relevant to a second-order moment closure of the flow, so the information presented also represents an archival database for model testing. The equations correspond to the specific configuration of the RT runs, with gravity acting in direction $i = 3$ and homogeneity assumed in the horizontal directions. All results presented here are obtained at the latest times in the two RT simulations. For clarity, some of the results have been smoothed by applying a running average.

The Favre mean and turbulent kinetic energy transport equations are

$$\frac{\partial}{\partial t}(\bar{\rho}\tilde{K}) = -(\bar{\rho}\tilde{U}_3\tilde{K})_{,3} - (\tilde{U}_3 R_{33})_{,3} + \bar{\rho}\tilde{U}_3 g_3$$
$$- \tilde{U}_3 P_{,3} + R_{33}\tilde{U}_{3,3} + \tilde{U}_3 \bar{\tau}_{33,3}, \qquad (16)$$

$$\frac{\partial}{\partial t}(\bar{\rho}\tilde{k}) = \underbrace{-(\bar{\rho}\tilde{U}_3\tilde{k})_{,3}}_{\text{I}} \underbrace{+a_3 P_{,3}}_{\text{II}} \underbrace{-R_{33}\tilde{U}_{3,3}}_{\text{III}} \underbrace{-a_3\bar{\tau}_{33,3}}_{\text{IV}} \underbrace{-\frac{1}{2}R_{ii3,3}}_{\text{V}}$$
$$\underbrace{-\langle u_3 p\rangle_{,3}}_{\text{VI}} \underbrace{+\langle u_i \tau_{i3}\rangle_{,3}}_{\text{VII}} \underbrace{+\langle pd\rangle}_{\text{VIII}} \underbrace{-\langle \tau_{ij}u_{i,j}\rangle}_{\text{IX}}. \qquad (17)$$

Figure 4 compares the main terms in the Favre turbulent kinetic energy equations between RT1 and RT2. In general, the results are qualitatively similar. Note that the kinetic energy itself is asymmetric in RT2 (see above); however, $\bar{\rho}\tilde{k}$ is close to symmetrical, together with most of the terms in its transport equation. The advection terms I and III, which are inherently asymmetric, are negligible near the Boussinesq limit. However, the turbulent transport term, term V, remains sizable at $A = 0.04$ and again dominates the energy balance near the edges of the layer. Note that at $A = 0.5$ the asymmetry of the advection terms is matched by an opposite asymmetry in the turbulent transport so that the overall balance remains symmetrical with respect to the centerline.
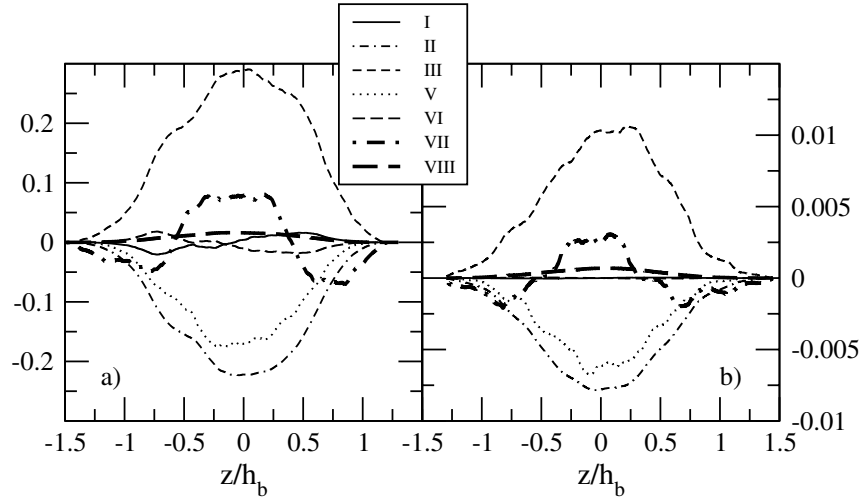
**Figure 5.** Terms in the mass flux equation, scaled by $\tau^2/L_0$, for (a) RT1 and (b) RT2.
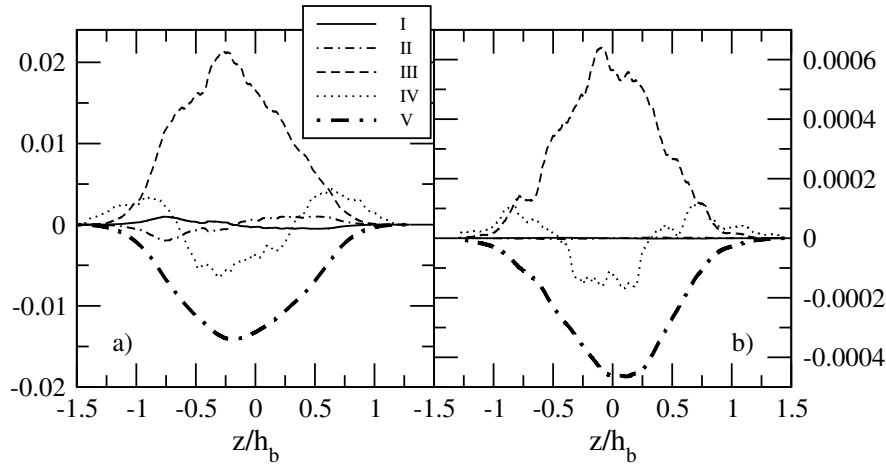


**Figure 6.** Terms in the equation for $b$, scaled by $\tau$, for (a) RT1 and (b) RT2.

The production term II in equation (17) depends on the mass flux and the mean pressure gradient. Since the mass flux is a second-order quantity, a moment closure at the second-order level requires a transport equation for $a_3$

$$
\frac{\partial}{\partial t}(\bar{\rho}a_3) = \underbrace{-(\bar{\rho}\tilde{U}_3 a_3)_{,3}}_{\text{I}} \underbrace{+b(P_{,3} - \bar{\tau}_{33,3})}_{\text{II}} \underbrace{+\bar{\rho}(\langle vp_{,3}\rangle - \langle v\tau_{3j,j}\rangle)}_{\text{III}}
$$

$$
\underbrace{-\bar{\rho}a_3(\tilde{U}_3 - a_3)_{,3}}_{\text{IV}} \underbrace{+\frac{\bar{\rho}_{,3}}{\bar{\rho}}(\langle \rho u_3^2\rangle - R_{33})}_{\text{V}} \underbrace{+\bar{\rho}(a_3^2)_{,3}}_{\text{VI}}
$$

$$
\underbrace{-\langle \rho u_3^2\rangle_{,3}}_{\text{VII}} \underbrace{-\bar{\rho}\langle u_3 d\rangle}_{\text{VIII}}. \tag{18}
$$

Again, barring the statistical variability, production, terms II and V, and destruction, term III, are symmetrical with respect to the centerline (figure 5). This is consistent with mass flux $\bar{\rho}a_3$ remaining symmetrical up to $A = 0.5$, as shown in [2]. The results obtained at $A = 0.5$ and $A = 0.04$ are qualitatively similar, except that the advection terms I and VI, which are asymmetrical, remain negligible at $A = 0.04$. Similar to the turbulent kinetic energy equation, turbulent transport, term VII, remains important near the Boussinesq limit.

Term II is the largest production term in equation (18). It depends on the mean pressure gradient and mixing state through density-specific volume covariance, $b$. The transport equation for $b$ is required in a moment closure at the second-order level.

$$
\frac{\partial}{\partial t}b = \underbrace{-\tilde{U}_3 b_{,3}}_{\text{I}} \underbrace{+2a_3 b_{,3}}_{\text{II}} \underbrace{-2a_3(1+b)\frac{\bar{\rho}_{,3}}{\bar{\rho}}}_{\text{III}}
$$

$$
\underbrace{+\bar{\rho}\left(\frac{\langle u_3 \rho v\rangle}{\bar{\rho}}\right)_{,3}}_{\text{IV}} \underbrace{+2\bar{\rho}\langle vd\rangle}_{\text{V}}. \tag{19}
$$

Unlike $\bar{\rho}\tilde{k}$ and $\bar{\rho}a_3$, $b$ is asymmetric at $A = 0.5$, a direct consequence of the mean density profile asymmetry. Thus, the results shown in figure 6 are qualitatively different in RT1 and RT2, because near the Boussinesq limit all the terms in equation (19) are close to symmetrical with respect to the centerline. In particular, this symmetry requires that the advection terms, I and II, are negligible at $A = 0.04$, similar to the results obtained for the other two moments equations considered. Again, the turbulent transport term IV remains important near the Boussinesq limit. The
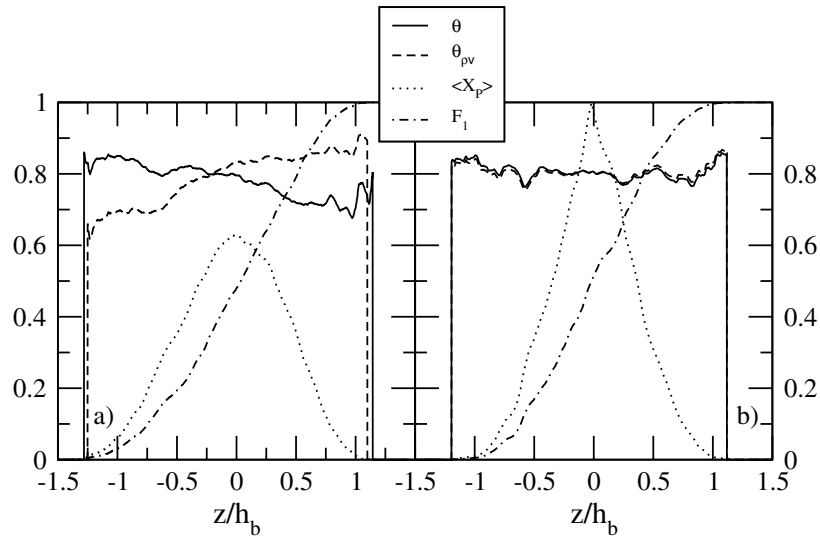
**Figure 7.** Several mix measures across the RT layer for (a) RT1 and (b) RT2.

importance of the turbulent transport in the second-order moments equations substantiates the significance of the slow rate for asymptotic self-similarity shown above. One of the main consequences, the lack of temporal self-similarity of the turbulent Reynolds number, renders the gradient diffusion hypothesis for the turbulent transport with the usual turbulence scales inappropriate for RT turbulence long after the onset of self-similar growth of the layer width.

## 4. Mixing state

Several metrics for assessing the state of the mixing will now be discussed. These metrics are compared in the context of the underlying density PDF and the question of how much pure and mixed fluids are in the field. All metrics are normalized to vary between 0 for a heterogeneous mixture of pure fluids and 1 for the fully mixed fluid.

In general, all mix metrics in use today for RT turbulence are constructed from lower-order moments of the density PDF. Thus, $\theta = \langle f_1 f_2 \rangle / F_1 F_2$, used in [23, 24], depends on the mean and variance of the density. While the density variance does appear in the dynamical equations in the Boussinesq limit [1], the VD moment equations do not contain any term depending on $\langle \rho^2 \rangle$. From the point of view of the dynamical equations, a more appropriate mix metric for the VD case would be constructed from density-specific volume covariance, $\theta_{\rho v} = 1 - b/b_{nm}$, where the no-mix value of $b$ is $b_{nm} = [(\bar{\rho} - \rho_1)(\rho_2 - \bar{\rho})]/\rho_1 \rho_2$. Figure 7 shows that the two metrics are close at $A = 0.04$, as expected, but they are different at $A = 0.5$. Thus, RT1 results indicate a qualitatively different behavior across the RT layer, as $\theta$ and $\theta_{\rho v}$ predict more mixing on the opposite sides of the layer. Nevertheless, both metrics have relatively large values across the whole layer, which is shown below to misrepresent the density PDF. Additionally, they cannot capture any asymmetry in the underlying PDF. Nevertheless, at higher $A$, the mixing becomes asymmetric even in the HRT case, which starts with a symmetrical density PDF [1]. Cook and Dimotakis [13] used a fast reaction analogy to calculate the average amount of completely mixed fluid, $\langle X_P \rangle$. Figure 7 shows that $\langle X_P \rangle$ better
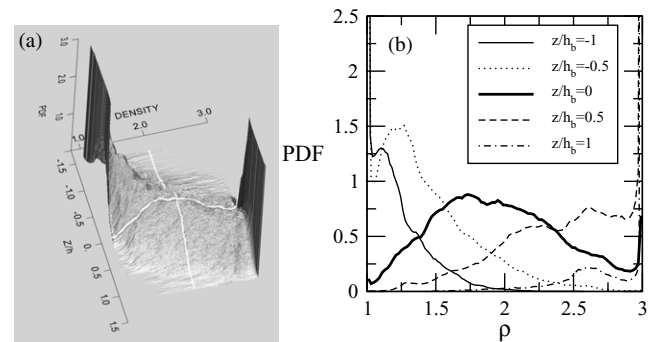


**Figure 8.** (a) Surface plot of density PDF and (b) density PDF at several locations across the layer in RT1, at the latest time in the simulation.

follows the expected behavior of the mixed fluid, although it can still not address any asymmetry in the density PDF and, in general, any information related to the pure or partially mixed fluid. Interestingly, at $A = 0.04$, $\langle X_P \rangle$ becomes close to 1.0 at the centerline, suggesting a homogeneous mixture with density close to $(\rho_1 + \rho_2)/2$ around the centerline. For reference, figure 7 also shows the variation of the mean volume fraction of the heavy fluid, $F_1$. Other mixing metrics proposed, for example the time-dependent Atwood number used in [25, 26], while useful in certain instances, are still only low-order representations of the underlying density PDF.

The density PDF shown in figure 8 for RT1 makes clear the limitations in evaluating the molecular mixing based on lower-moment metrics like $\theta$. At the top of the layer the PDF is spiked at the heavy fluid end and includes some partially mixed fluid. At the bottom of the layer the PDF is spiked at the light fluid with some partially mixed fluid. The transition from one side to the other is also not monotonic. Yet, across the layer $\theta$ varies slowly not in any way giving a notion as to the radically different amounts of pure or mixed fluid. See [24, 27] for examples of such PDFs given by coarse-grained simulations. Livescu and Ristorcelli [1] provide rigorous bounds on the pure and the mixed fluid based on several mix metrics. These bounds emphasize the
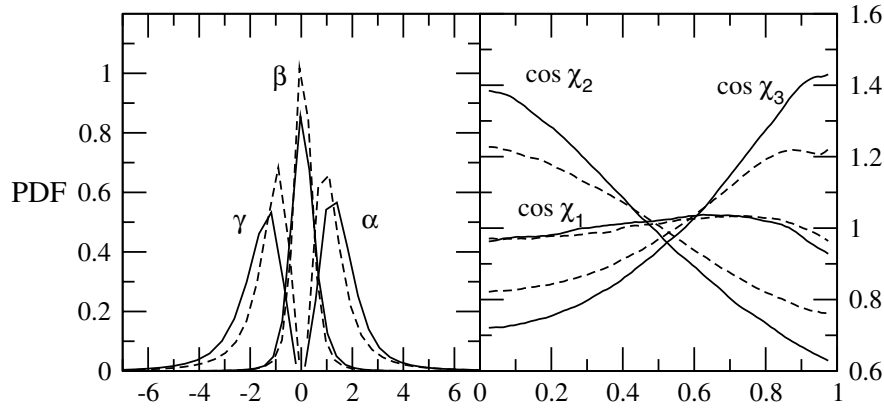
**Figure 9.** PDFs of the (a) eigenvalues of $s_{ij}$ and (b) cosines of the angles between $\nabla\rho$ and the eigenvectors of $s_{ij}$ in the light fluid, $\rho < \overline{\rho}$ (continuous lines), and heavy fluid, $\rho > \overline{\rho}$ (dashed lines), at $A = 0.5$.

uncertainty in knowing the underlying mixing state when only lower-moment metrics are specified.

The density PDF at the centerline of the RT1 simulation also has an interesting behavior, first observed in HRT [1]: the PDF is not symmetrical. The peak is at $\rho < 2$ and the amount of pure heavy fluid is larger than that of pure light fluid. As a result, the penetration distance of the pure heavy fluid is longer than that of the pure light fluid. Thus, similar to HRT, the two pure fluids mix at different rates in the VD case.

In HRT, the density PDF starts as a double delta and then evolves towards a single peaked PDF as the fluids become molecularly mixed. At low $A$, near the Boussinesq approximation, the PDF remains symmetrical at all times [1]. At higher $A$, the PDF becomes rapidly skewed as the two pure fluids mix at different rates, with the pure light fluid mixing faster than the pure heavy fluid.

Below, we provide an explanation for this mixing asymmetry, using HRT data (see also [28]). The asymmetry of the density PDF in the VD case can be understood from the skewness, $S \equiv \langle \rho^3 \rangle / (\langle \rho^2 \rangle^{3/2})$, equation

$$\frac{\mathrm{d}}{\mathrm{d}t} S = 6 \frac{\langle \rho_{,k} \rho_{,k} \rangle}{Re_0 Sc} \left( \frac{S}{2\langle \rho^2 \rangle} - \frac{\langle \rho \rho_{,j} \rho_{,j} \rangle}{\langle \rho_{,k} \rho_{,k} \rangle \langle \rho^2 \rangle^{1/2}} \right). \quad (20)$$

As the flow begins with $S = 0$, it is the second term, the production, that generates the skewness of the PDF. The quantity $\langle \rho \rho_{,j} \rho_{,j} \rangle$ is weighted towards large squared density gradient events occurring in lower than average density regions so that $S > 0$ at early times. In other words, the light fluid blobs become more fragmented at higher $A$. As the mixing proceeds, the production term and the magnitude of the density gradient approach zero and the rate of change of the skewness becomes small.

The density PDF skewness generation mechanism, $\langle \rho \rho_{,j} \rho_{,j} \rangle$, is determined, through changes in the magnitude of the density gradient, by the eigenvalues of the strain rate tensor, $s_{ij} = (u_{i,j} + u_{j,i})/2$, and the relative alignment between $\nabla\rho$ and the eigenvectors of $s_{ij}$:

$$\frac{\mathrm{d}}{\mathrm{d}t} \langle \rho_{,j} \rho_{,j} \rangle = -2\langle \rho_{,i} s_{ij} \rho_{,j} \rangle + \langle u_{i,i}(\rho_{,j}\rho_{,j} + 2\rho^*\rho_{,jj}) \rangle, \quad (21)$$

where the second term, which depends on the velocity divergence, is small after the initial transients. Let $\chi_1$, $\chi_2$ and $\chi_3$ be the angles between $\nabla\rho$ and the $\alpha$-, $\beta$- and

$\gamma$-eigenvectors, which correspond to the eigenvalues labelled using the usual convention $\alpha > \beta > \gamma$. In isotropic turbulence, it is known that passive scalar gradients tend to align with the most compressive ($\gamma$) eigenvector of $s_{ij}$ [29]. Similar results are obtained in HRT; however, there are important differences between the low and high $A$ cases:

- *Low A*: the relative alignment and the magnitude of the eigenvectors are about the same in the light and heavy fluid regions.
- *High A*: both the eigenvalues and the alignment of $\nabla\rho$ with the principal axes of $s_{ij}$ are different in the light and heavy fluids (figure 9).

In the light fluid, the eigenvalues $\alpha$ and $\gamma$ have larger magnitudes as the reduced inertia allows higher deformation rates of a fluid particle. Moreover, the alignment of $\nabla\rho$ with the $\gamma$-eigenvector weakens in the heavy fluid regions, as the inertia of the heavy fluid particles tends to make them less responsive to deformations due to local strain. Thus, the local structure of the flow changes in response to the inertia of the fluid particles. The net result is a decrease in the magnitude of $\langle \rho_{,j} s_{ij} \rho_{,j} \rangle$ (note that this quantity has negative sign) in the heavy fluid regions compared to the light fluid regions. Consequently, the inertia of the heavy fluid inhibits the growth of the density gradients and reduces the rate at which heavy fluid regions are broken up by stirring, ultimately leading to reduced mixing.

## 5. Summary and conclusions

An overview of turbulence and turbulent mixing characteristics in buoyancy-driven flows with moderate VD effects has been provided using the largest data sets available in two unit configurations: classical RT instability and an idealized triply periodic buoyancy-driven flow. For the RT case, with a $3072^3$ data set, $A = 0.5$, the simulation of Cabot and Cook [4], further analyzed in [2], has been compared to a new simulation, at $A = 0.04$, on a $1024^2 \times 4032$ mesh. For the HRT case, the simulations used cover the range $A = 0.05$–$0.5$, on up to $1024^3$ meshes.

The results discussed in this study can be divided into three main categories: (i) the marked difference in the mixing between different density fluids as opposed to mixing that occurs between fluids of commensurate

densities, corresponding to the Boussinesq approximation; (ii) anomalous small-scale anisotropy persistence at small Atwood numbers; and (iii) the different rates of approach to self-similarity for different classes of quantities and the implications for turbulence models.

The main points of the paper can be summarized as follows:

- *Mixing asymmetry.* Mixing is qualitatively different in VD flows compared to the Boussinesq limit, with the pure heavy fluid mixing more slowly than the pure light fluid. Thus, in HRT, an initially symmetric density PDF develops a marked skewness. One consequence for the RT layer is that penetration distance of the pure heavy fluid is larger than that of the pure light fluid. None of the mix metrics currently used for RT turbulence, e.g. $\theta$, can capture this asymmetry. A mechanism producing the mixing asymmetry, based on the changes in local structure of the flow in response to the fluid inertia, has been proposed.

- *VD mixing and the asymmetry of the turbulence statistics.* At moderate $A$, the turbulence, as reflected in the Favre turbulent kinetic energy and mean velocity, normalized mass flux and density-specific volume covariance, develops asymmetry across the RT layer related to that of the mean density profile. This is a consequence of the behavior of the mean density profile in the interior of the RT layer.

- *Anomalous small-scale anisotropy.* The scale dependence of the normal stresses anisotropy indicates anomalous anisotropy at small scales, even though the flow becomes close to isotropic at intermediate scales. The results hold both near the Boussinesq limit and at $A = 0.5$.

- *Slow approach to the self-similarity of derived turbulence quantities.* Although the RT layer width growth becomes self-similar relatively fast, full or asymptotic self-similarity (such that a single lengthscale describes the flow) takes a much longer time to achieve. For the duration of RT1 and a significant part of RT2, the lower-order terms in the self-similar expressions for the large- and small-scale primitive quantities remain mismatched. As a consequence, derived quantities, such as the turbulent Reynolds number or turbulence lengthscale, are slow to reach self-similarity, in contradistinction to primitive quantities, such as kinetic energy. Since $Re_t$ is proportional to the eddy diffusivity in the popular gradient diffusion hypothesis, the results indicate that the current turbulent transport models cannot be used before the asymptotic self-similar state is reached and that self-similarity of the layer width growth is a poor indicator of reaching this state.

In addition, the energy budgets for the Favre turbulent kinetic energy, mass flux and density-specific volume correlation transport equations, relevant to a second-order moment closure of the flow, have been provided as an archival database for model testing.

The paper discusses some unexpected new physics associated with buoyancy and VD effects. It would be interesting to know how (and if) the findings would change at even higher $A$ and/or Reynolds numbers. This question is being addressed with higher-resolution simulations, currently under way.

## Acknowledgments

## References

[1] Livescu D and Ristorcelli J R 2008 Variable-density mixing in buoyancy-driven turbulence *J. Fluid Mech.* **605** 145–80

[2] Livescu D, Ristorcelli J R, Gore R A, Dean S H, Cabot W H and Cook A W 2008 High-Reynolds number Rayleigh–Taylor turbulence *J. Turbul.* **10** 1–32

[3] Livescu D and Ristorcelli J R 2007 Buoyancy-driven variable-density turbulence *J. Fluid Mech.* **591** 43–71

[4] Cabot W H and Cook A W 2006 Reynolds number effects on Rayleigh–Taylor instability with possible implications for type-ia supernovae *Nat. Phys.* **2** 562–8

[5] Dalziel S B, Linden P F and Youngs D L 1999 Self-similarity and internal structure of turbulence induced by Rayleigh–Taylor instability *J. Fluid Mech.* **399** 1–48

[6] Young Y N, Tufo H, Dubey A and Rosner R 1999 On the miscible Rayleigh–Taylor instability: two and three dimensions *J. Fluid Mech.* **447** 377–408

[7] Dimonte G and Schneider M 2000 Density ratio dependence of Rayleigh–Taylor mixing for sustained and impulsive acceleration histories *Phys. Fluids* **12** 304–21

[8] Dimonte G *et al* 2004 A comparative study of the turbulent Rayleigh–Taylor instability using high-resolution three-dimensional numerical simulations: the Alpha-Group collaboration *Phys. Fluids* **16** 1668–92

[9] Ristorcelli J R and Clark T T 2004 Rayleigh–Taylor turbulence: self-similar analysis and direct numerical simulations *J. Fluid Mech.* **507** 213–53

[10] Ramaprabhu P, Dimonte G and Andrews M J 2005 A numerical study of the influence of initial perturbations on the turbulent Rayleigh–Taylor instability *J. Fluid Mech.* **536** 285–319

[11] Muenshke N J, Schilling O, Youngs D L and Andrews M J 2009 Measurements of molecular mixing in a high-Schmidt-number Rayleigh–Taylor *J. Fluid Mech.* **632** 17–48

[12] Youngs D L 2009 Application of monotone integrated large eddy simulation to Rayleigh–Taylor mixing *Phil. Trans. R. Soc.* A **367** 2971–83

[13] Cook A W and Dimotakis P E 2001 Transition stages of Rayleigh–Taylor instability between miscible fluids *J. Fluid Mech.* **443** 69–99

[14] Cook A W, Cabot W H and Miller P L 2004 The mixing transition in Rayleigh–Taylor instability *J. Fluid Mech.* **511** 333–62

[15] Chung D and Pullin D I 2010 Direct numerical simulation and large-eddy simulation of stationary buoyancy-driven turbulence *J. Fluid Mech.* **643** 279–308

[16] Livescu D, Khang Y, Mohd-Yusof J, Petersen M R and Grove J W 2009 CFDNS: a computer code for direct numerical simulation of turbulent flows *Technical Report* LA-CC-09-100 Los Alamos National Laboratory

[17] Lele S K 1992 Compact finite difference schemes with spectral-like resolution *J. Comput. Phys.* **103** 16–42

[18] Petersen M R and Livescu D 2010 Forcing for statistically stationary compressible isotropic turbulence *Phys. Fluids* at press

[19] Banerjee A and Andrews M J 2009 3-d simulations to investigate the initial conditions effects on the growth of Rayleigh–Taylor mixing *Int. J. Heat Mass Transfer* **52** 3906–17

[20] Youngs D L 1984 Numerical simulation of turbulent mixing by Rayleigh–Taylor instability *Physica* D **12** 32–44

[21] Read K I 1984 Experimental investigation of turbulent mixing by Rayleigh–Taylor instability *Physica* D **12** 45–58

[22] Andrews M J and Spalding D B 1990 A simple experiment to investigate two-dimensional mixing by Rayleigh–Taylor instability *Phys. Fluids* A **2** 922–7

[23] Youngs D L 1991 Three-dimensional numerical simulation of turbulent mixing by Rayleigh–Taylor instability *Phys. Fluids* A **3** 1312–20

[24] Linden P F, Redondo J M and Youngs D L 1994 Molecular mixing in Rayleigh–Taylor instability *J. Fluid Mech.* **265** 97–124

[25] George E and Glimm J 2005 Self-similarity of Rayleigh–Taylor mixing rates *Phys. Fluids* **17** 054101

[26] Liu X, George E, Bo W and Glimm J 2006 Turbulent mixing with physical mass diffusion *Phys. Rev.* E **73** 016304

[27] Youngs D L 1994 Numerical simulation of mixing in Rayleigh–Taylor and Richtmeyer–Meshkov instabilities *Laser Part. Beams* **12** 725–50

[28] Livescu D and Ristorcelli J R 2010 Mixing asymmetry in variable density turbulence *Advances in turbulence XII* vol 132 (Berlin: Springer) pp 545–8

[29] Jaberi F A, Livescu D and Madnia C K 2000 Characteristics of chemically reacting compressible homogeneous turbulence *Phys. Fluids* **12** 1189–209